

Research Article

High-Precision Electrical Impedance Tomography for Electrical Conductivity of Metallic Materials

Shuanfeng Zhao , **Yao Miao**, **Rongxia Chai**, **Jiaojiao Zhao**, **Yunrui Bai**, **Zheng Wei**,
and **Simin Ren**

School of Mechanical Engineering, Xi'an University of Science and Technology, Xi'an 710054, China

Correspondence should be addressed to Shuanfeng Zhao; zsf@xust.edu.cn

Received 16 October 2021; Accepted 16 February 2022; Published 15 March 2022

Academic Editor: Gianfranco Carotenuto

Copyright © 2022 Shuanfeng Zhao et al. This is an open access article distributed under the Creative Commons Attribution License, which permits unrestricted use, distribution, and reproduction in any medium, provided the original work is properly cited.

Metal materials are subject to deformation, internal stress distribution, and cracking during processing, all of which affect the distribution of electrical conductivity of the metal. Suppose we can detect the conductivity distribution of metal materials in real time. In that case, we can complete the inverse imaging of metal material properties, structures, cracks, etc. and realize non-destructive flaw detection. However, metal materials' small resistance, high electrical conductivity, and susceptibility of voltage signals to noise signal interference make an accurate measurement of metal conductivity challenging. Therefore, this paper addresses the problem of detecting the conductivity distribution of metals by investigating a high-precision four-electrode AC measurement method. This technical approach combines laminar imaging techniques with high-precision weak signal extraction methods. On this basis, a method and equipment for high-precision electrical impedance tomography of metallic materials' electrical conductivity were established. The way specifies a new number of electrodes and adopts a model of spaced excitation reference measurements. Single-frequency sinusoidal AC signal is used for excitation, and Shannon wavelet analysis is used for signal extraction and noise reduction. Super-resolution reconstruction algorithms are used for resistivity distribution image reconstruction to improve image quality. Based on the results of various comparative experiments, it is clear that this new functional technique method has good imaging stability and operability and can perform tasks such as analyzing the internal conductivity distribution of metals. This research provides an effective way of new ideas for the safe detection of metal structures, the changes in crystal tissue structure, and the study of metal properties. In particular, it expands the scope of research in the development and application of resistance tomography, which has tremendous commercial potential research significance.

1. Introduction

Changes in external factors such as deformation and heat to the metal will cause changes in the lattice composition or metallographic organization, which will result in changes in the electrical conductivity of the metal. Based on the above metal properties, it is known that the resistivity of the strange metal region will have a significant variation. However, unlike conventional nonconductors, metallic materials are good conductors with very low resistivity [1]. This makes the inductive electromotive force generated at energization higher than the measurement signal, making measurement very difficult. Therefore, it is very challenging to extract tiny

signals under high noise conditions. Conventional resistive tomography techniques are typically used in subjects with high resistivities, such as lung imaging [2]. For metallic materials with small resistivity, this paper assigns frequency characteristics to the excitation current signal by single-frequency AC excitation. Then, the Shannon wavelet extracts the feature signal to complete the work of removing the tiny measurement signal in the case of solid noise. Finally, the electrical impedance tomography of the metal conductivity is completed.

For example, Mandal et al. studied radiation detectors and measured object voltage signals [3]. At present, domestic and foreign measuring instruments of this type are

expensive and have low accuracy. Its function is limited to the measurement of resistance, and this paper goes deeper to study the resistivity distribution. Milne and Carter proposed detecting metals by thermal waves, which can detect the thickness of metal media and the distribution of internal defects. Infrared thermography requires a high level of the external environment and detection equipment, and the detection results are easily affected by the external environment [4]. Zhao et al. completed the overdetection of coal mine inclined shafts by measuring the soil conductivity [5, 6]. However, the objects studied in these studies were nonmetallic objects or susceptible to environmental influences. Traditional crack detection techniques such as ultrasonic and radiographic detection apply to the overall detection of macroscopic aspects. With the trend towards high precision in industrial technology, metallic materials have become more demanding in detecting defects in microscopic crystal organization and presenting the results in the form of images. This facilitates timely understanding of the location of faults and rapid remedial action.

Electrical resistance tomography (ERT) as an imaging method for structural health inspection has been widely used in various research fields [7]. Many scholars have investigated ERT technology from several aspects. For example, in the area of geological assessment, it can detect and analyze subsurface rock structures [8], primarily historical and cultural monuments [9], and observe the migration of subsurface water in the soil [10, 11]. In biomedical applications, ERT technology is often used to detect the lung region. In industrial engineering, ERT is used to evaluate different pipes and various tanks to observe liquid-solid and gas-liquid-solid processes [12], as well as composite structure imaging [13] and bone cement imaging [14], among many other applications. China University of Mining and Technology completed a study on detecting soil resistivity using ERT technology [15]. Karhunen et al. performed electrical resistance tomography imaging tests on cement mortar specimens containing cracks, reinforcement, and holes. They succeeded in accurately locating damage such as reinforcement, cracks, and gaps within the models, verifying the feasibility of the ERT technique in terms of damage detection [16]. The ERT method also allows quantitative evaluation in nonionic solutions [17] and monitoring of crystallization processes [18]. For example, Boulanger studied the crystallization process of low conductivity solutions by the ERT technique [19]. These applications demonstrate that ERT imaging can be accomplished in low conductivity environments with different spatial dimensions and different conductivity distributions in the target region. Meanwhile, resistance tomography imaging systems have been widely used. To ensure the safety of metal structures and reduce the occurrence of engineering accidents, this paper explores and investigates the application of ERT technology to the nondestructive testing of high conductivity metal materials.

Therefore, we propose an ERT metal detection method and device. The new plan aims to improve the traditional ERT method by combining the properties of metallic materials: First, the new way is not to study and analyze a

specific influencing factor, but to optimize the hardware and reconstruction algorithm of traditional ERT around the research object, to achieve the purpose of detecting the internal structure of the metal. In signal acquisition and processing, Hornik et al. studied voltage signal acquisition considering only the problem of sensitive field voltage variation [20], ignoring the effect of other factors such as voltage signal distortion on raw data variation during the acquisition process. In this paper, the input impedance is increased by differential acquisition when acquiring voltage signals—measurement acquisition of small voltage signal data based on the subtraction of two calls to reduce common-mode interference. Based on the relationship between current and voltage, the RMS value of the voltage signal is calculated, and all RMS values are formed into a measurement array to provide data support for the inversion work. Regarding noise reduction of measurement data, when a metallic material of a good conductor is in a complex electromagnetic environment, the surface generates an induced electric potential higher than the excitation signal as an interference signal. The noise signal can reach the volt unit level when the RMS value of the measured signal is the nanovolt unit level. Therefore, how to extract the metal object measurement signal under high noise conditions is the first problem to be solved. Kolehmainen et al. studied the discomfort and inverse problems of the reconstruction algorithm. They did a sensitivity analysis of the noise and numerical errors in the experimental voltage signal data [21]. This paper addresses this problem by proposing a specific frequency AC signal as the excitation signal, which effectively solves the problem that the DC excitation signal is difficult to extract directly and prone to polarization effect. At the same time, this paper removes the single-frequency components of the measured signal using signal analysis to achieve noise separation. The single-frequency components are extracted using the Shannon wavelet method to complete the single frequency feature analysis. In terms of image reconstruction, conductivity σ was elaborated in an inverse problem study by Ciulli et al. [22]. Martins et al. investigated the inverse problem in the reconstruction algorithm. They analyzed the inverse problem by solving the positive problem and the potential measurements on the surface of the object under study [23]. In this paper, the inverse problem of ERT is modelled and analyzed for research and image reconstruction. Meanwhile, to reduce the influence of measurement resistance, this paper invokes the super-resolution resistance tomography method to improve the quality of reconstructed images. Super-resolution reconstruction is a process of extracting feature information of the study object from many low-resolution images of traditional reconstruction algorithms and generating high-resolution images after several iterations. In summary, the contributions of this paper are fourfold:

- (1) A novel high-precision chromatographic imaging technique is proposed, and a high-precision electrical impedance tomography device for electrical conductivity of metallic materials is developed.

- (2) A Shannon wavelet extraction measurement signal technique is proposed; while selecting a single frequency sinusoidal AC signal as the excitation, the noise reduction problem of the measurement signal is solved.
- (3) The laminar imaging technique is combined with a high-precision weak signal extraction method, and a new mode of electrode number and interval excitation reference measurement is specified. Meanwhile, the electric field distribution model for each excitation mode is established.
- (4) In the image reconstruction technique, super-resolution reconstruction algorithms are used to improve the accuracy of the reconstructed images.

The rest of this paper is organized as follows. Section 2 describes the principle of the ERT system to provide a theoretical basis for the high-precision laminar imaging technique for the resistivity of metallic materials. Based on the comparative analysis of experimental results, Section 3 discusses the relationship between data noise reduction, number of electrodes, excitation measurement mode, super-resolution reconstruction method, and measurement data. The analysis of the experimental temperature results is discussed in Section 3.3. Finally, Sections 4 and 5 discuss and give concluding remarks and suggestions for future work.

2. Materials and Methods

2.1. Basic Principles of Metal Conductivity Chromatography Imaging. Conductivity tomography is one of the electrical detection techniques, which has the advantages of visualization, noninvasiveness, low cost, and high accuracy. Conductivity is one of the critical physical parameters of metals. When the sensitive field medium distribution of the study object changes, the conductivity distribution within the field will change simultaneously.

Figure 1 shows the block diagram of the metal conductivity electrical resistance tomography system. As shown in the figure, the ERT system in this paper mainly includes [24] sensitive field electrode array, single frequency AC excitation unit, weak signal amplification unit, data acquisition and processing unit, and image reconstruction unit. Among them, the image reconstruction unit contains Shannon wavelet analysis and super-resolution image reconstruction. First, the single-frequency AC excitation unit generates a single-frequency excitation current with a characteristic signal, which is fed into the metal-sensitive field through the electrode array. The weak signal amplification unit improves weak feature signals, which are passed to the data processing post-acquisition and processing unit after the initial filtering and amplification process. Then, the noise reduction of the data and the extraction of feature signals are made by Shannon wavelet analysis to reach the information of the internal conductivity distribution of the metal. Finally, the image reconstruction unit reconstructs the media distribution image based on this to visualize the internal structure of the metal [25].

Figure 2 shows the block diagram of excitation and measurement electrode switching selection. The signal source generates a sine wave signal as the control signal of the voltage-controlled constant-current source module, which will output the sinusoidal AC power required after conversion by the voltage-controlled constant-current source module [26]. The signal source program controls the frequency of the sinusoidal voltage signal. The voltage-controlled current source circuit converts the output sinusoidal voltage signal into the sinusoidal current signal required by the system [27]. The ADG1406 high-speed analogue toggle switch is a chip for switching electrodes with a fast switching speed of about 10 ns. The switching circuit consists of a total of 4 pieces of ADG1406 [28]. The data acquisition and processing unit is the central part of the ERT system. The weak signal amplification unit adjusts the gain to enable better data processing by the conditioning circuit in the later stage [29]. This unit is responsible for acquiring the weak output voltage signal in the measurement electrode array, completing the processing, and then sending the received data signal to the host computer to complete the image reconstruction [30, 31].

For metals, the resistivity comes mainly from the scattering effect of lattice vibrations on electrons. Suppose that the phonon system consists of so-called average phonons. The momentum of each photon is equal to the average rate of the phonons in the original electronic system. Although there are many electrons in the metal, it is only the electrons near the Fermi surface that are involved in conducting electricity.

$$\frac{1}{\tau_F} = Z\Theta(\bar{k}', \bar{k}, \bar{\theta})(1 - \cos \bar{\theta}), \quad (1)$$

where Z is a constant representing the sum of the electronic states other than the K state on the Fermi surface, $\bar{\theta}$ is the scattering angle resulting from electron scattering action, and $\Theta(\bar{k}', \bar{k}, \bar{\theta})$ is the collision probability of electrons with phonons.

$$\Theta(\bar{k}', \bar{k}, \bar{\theta})\mu\bar{v}, \bar{n}, \quad (2)$$

where \bar{v} is the average relative velocity of electrons and phonons near the Fermi surface. The number of collisions between a certain A molecule and B molecule per unit time is directly proportional to the relative velocities of A and B and the concentration of B molecules.

The presence of impurities and defects in the actual material affects the periodic potential field and causes the scattering of electrons. Small impurity concentrations, the lattice vibrations, and the distribution of impurities and defects are independent. The sum of the total scattering probabilities can be expressed in terms of the chirality time as

$$\frac{1}{\tau} = \frac{1}{\tau_L} + \frac{1}{\tau_r}. \quad (3)$$

$1/\tau_L$ denotes the contribution of lattice vibration scattering. $1/\tau_r$ denotes the contribution of impurity and defect scattering.

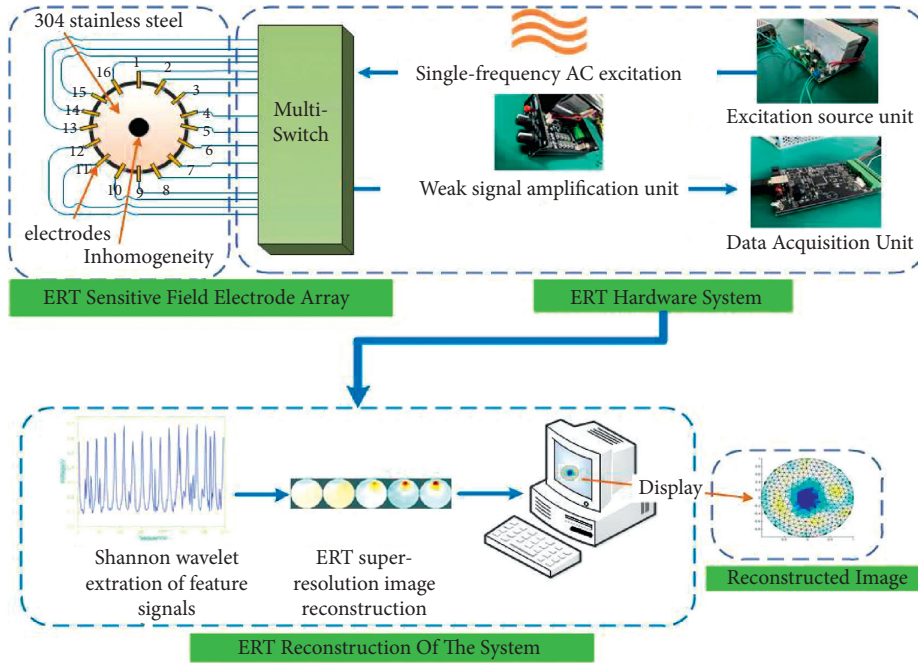


FIGURE 1: Block diagram of metal conductivity electrical resistance tomography system.

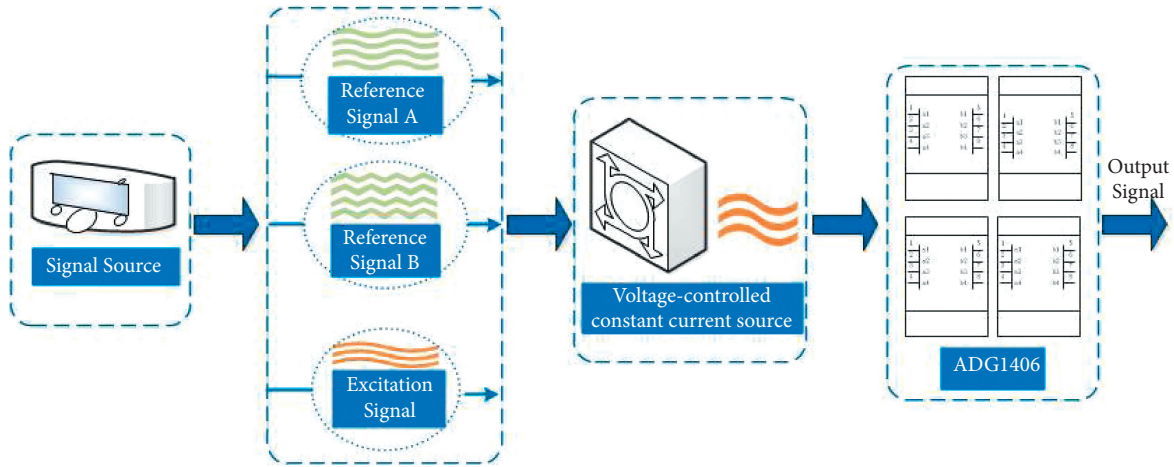


FIGURE 2: Block diagram of excitation and measurement electrode switching selection.

$$\rho = \rho_L + \rho_r, \tag{4}$$

where ρ_L represents the resistivity of the pure metal and ρ_r indicates the effect of scattering of impurities and defects and is temperature-dependent. When T is stable, ρ_L is 0 and ρ_r is the residual resistivity of the metal. Therefore, the presence of impurities and defects can change the value of metal resistivity. When the atomic spacing is changed, the energy band structure is changed, and the internal weaknesses and electronic form are changed, thus affecting the electrical conductivity of the metal.

2.2. Mathematical Model for Metal Conductivity Tomography

2.2.1. Positive Problem. The reconstruction method for reconstructing the conductivity distribution inside a metal is

essentially an ill-posed problem: the positive and the inverse problem. The inverse problem of ERT is solved, which requires a positive problem model [32, 33]. In the forward problem, the electric field, boundary conditions, and assumed conductivity distribution in the geometric region of the object of study are obtained.

Figure 3 shows a two-dimensional illustration of the heterogeneous body problem in electrical impedance tomography. Observing the two-dimensional region Ω and the boundary region $\partial\Omega$, it is assumed that the positive problem of quasi-static charge distribution allows obtaining a partial differential equation to model the two-dimensional region Ω , which can be expressed as

$$\vec{\nabla} \cdot (\sigma \vec{\nabla} u) = 0, \tag{5}$$

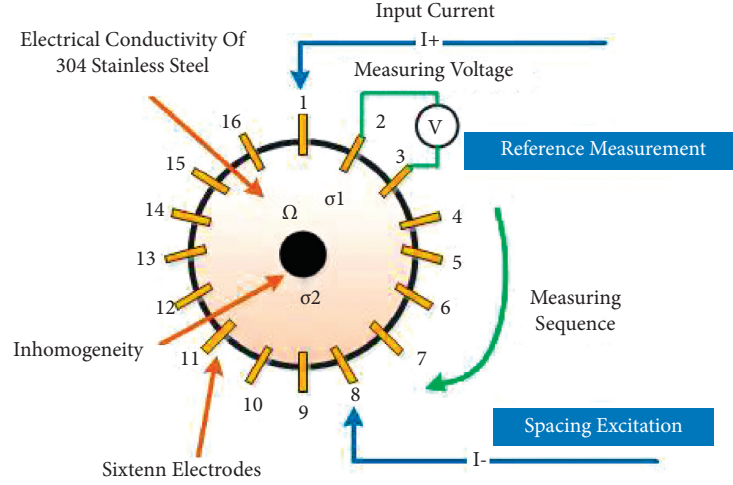


FIGURE 3: Two-dimensional illustration of the heterogeneous body problem in electrical impedance tomography.

where u is the electric potential and σ is the internal conductivity of the two-dimensional region Ω . Based on the seemingly stable field theory and combined with Maxwell's equation, a mathematical model of the electrical orthogonality of the metal structure is established as follows:

$$\begin{cases} \nabla \times H = J + \frac{\partial Y}{\partial t}, \\ \nabla \times E = -\frac{\partial B}{\partial t}, \\ \nabla \cdot B = 0, \\ \nabla \cdot Y = \rho_e, \end{cases} \quad (6)$$

where H represents the magnetic field strength; J represents the current density; E represents the electric field strength; Y represents the potential shift vector; ρ_e represents the charge density; and B represents the magnetic induction strength. Maxwell's system of differential equations is used to model the positive electrical problem of metallic materials. The positive problem model is built and solved using the finite element method to provide a computational model for the subsequent inverse problem algorithm.

2.2.2. Inverse Problem. There is no unique solution to the inverse problem, and small changes in the data can lead to significant changes in the reconstructed image [34]. Figure 4 illustrates the process of solving the ERT inverse problem.

The observational model for the process of solving the positive metal conductivity problem is expressed as

$$V = L(\sigma), \quad (7)$$

where V denotes the measured voltage vector at the electrode and σ indicates the conductivity of the metal in the

detection zone. The relationship between the change in conductivity $\Delta\sigma$ and the change in voltage ΔV can be expressed as

$$\Delta V = \frac{\partial L}{\partial \sigma} (\Delta\sigma) + o((\Delta\sigma)^2). \quad (8)$$

It is known during the forward simulation that the value of $\Delta\sigma$ is generally small, so the higher-order terms obtained from the expansion can be neglected, where $\partial L/\partial\sigma$ is called the sensitivity matrix and can be represented by W . (8) can be expressed as

$$\Delta V = \frac{\partial L}{\partial \sigma} \Delta\sigma = W \Delta\sigma. \quad (9)$$

Dividing the sensitive field region into m cells, if k independent measured voltage data are obtained, the discretized and normalized (9) can be expressed as

$$U = W \cdot G. \quad (10)$$

The equation of the inversion process can be expressed as

$$G = W^{-1} \cdot U. \quad (11)$$

where G is the conductivity distribution with dimension $m \times 1$, U is the measured voltage vector with dimension $k \times 1$, and W is the $k \times m$ dimensional sensitivity matrix.

The reconstruction algorithm for the super-resolution inverse problem is used to solve the static measurement problem in ERT [35]. The equation of the objective function $\varphi(\rho)$ can be expressed as

$$\varphi(\rho) = \frac{1}{2} \left\{ \|u(\rho) - V\|^2 + \alpha \|R_\rho\|^2 \right\}, \quad (12)$$

where $\varphi(\rho)$, $u(\rho)$ is the calculated voltage, V is the measured voltage, ρ is the matrix, and α is the regularization parameter.

Figure 5 shows the schematic diagram of the super-resolution reconstructed image. Super-resolution image reconstruction obtains feature information from low-resolution images of traditional reconstruction algorithms and

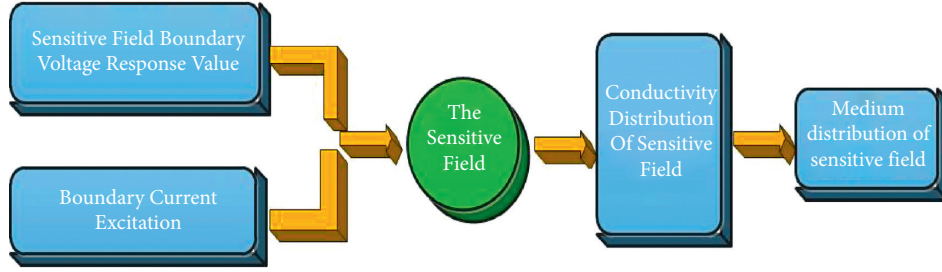


FIGURE 4: ERT inverse problem-solving process diagram.

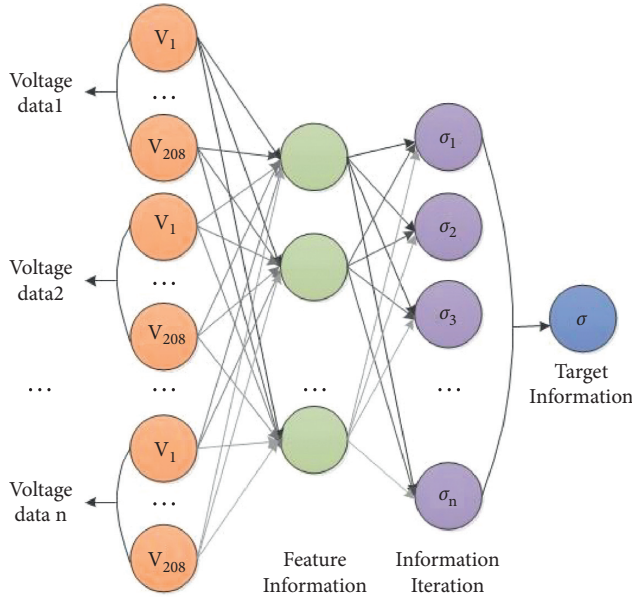


FIGURE 5: Schematic diagram of the super-resolution reconstructed image.

generates high-resolution images after several iterations. The image acquisition process at a discrete moment t is expressed as

$$y(t) = DH x(t) + e(t), \quad (13)$$

where $y(t)$ and $x(t)$ denote the vectorized representations of the degraded image and the original image, respectively; D denotes the quadratic sampling modeling matrix; H denotes the fuzzy modeling matrix during acquisition; and $e(t)$ denotes the noise model.

The total change in conductivity is defined as [36]

$$TV(\sigma) = \int_{\Omega} |(\nabla\sigma)|d\Omega, \quad (14)$$

where σ is the conductivity vector and $d\Omega$ is the area to be imaged. In static image reconstruction, the goal is to obtain the electrical conductivity of the analyzed area.

2.3. Modeling Study of Metal Conductivity Chromatography Imaging. ERT techniques have been used for qualitative imaging, especially for simulation studies of quantitative information [37]. In this paper, a disc model with a diameter

of 30 mm is evaluated and studied and segmented in different iterations using an adaptive threshold segmentation method [38]. Figure 6 shows the modeling diagram of the forward and reverse problems.

Figure 7 shows the different finite element meshes generated [39–42]. The finite element model is obtained after the grid dissection of the ERT sensitive field. The limited element model grid image affects data analysis progress, and numerous triangular domain cells and boundary cells form the complete grid [43]. With the gradual denseness of the mesh profile and the gradual increase in the number of meshes, the data obtained from the simulation will be closer to the actual results.

3. Experiment

In this paper, a series of experiments are designed to verify the accuracy of the proposed method, and some factors affecting the reconstruction results are discussed. The experiments are summarized in Table 1.

3.1. Experimental Platform Design. In this paper, an experimental platform is designed to test and verify the metal conductivity tomography imaging system's central performance, which leads to ascertaining the proposed method's feasibility in this paper. The total surface area of the electrode in contact with the medium is 19.63 mm² square. The measured dimensions of the experimental material are shown in Table 2.

The experimental platform is shown in Figure 8. The excitation unit provides a sinusoidal AC voltage value signal rated at 75 Hz to excite the electrodes sequentially. A voltage-current evaluation method and current excitation voltage measurements were chosen for the experiments, and the electrodes cycled through this acquisition process sequentially and recorded data frames [44]. The data acquisition and processing unit acquire the voltage signal at a frequency of 1 kHz. The voltage signal data is transmitted to a computer via a serial line connection and used to reconstruct still images.

3.2. Influencing Factors and Discussion

3.2.1. Data Noise Reduction. The voltage signal received by the data acquisition module contains many interference signals that directly affect the collected voltage signal,

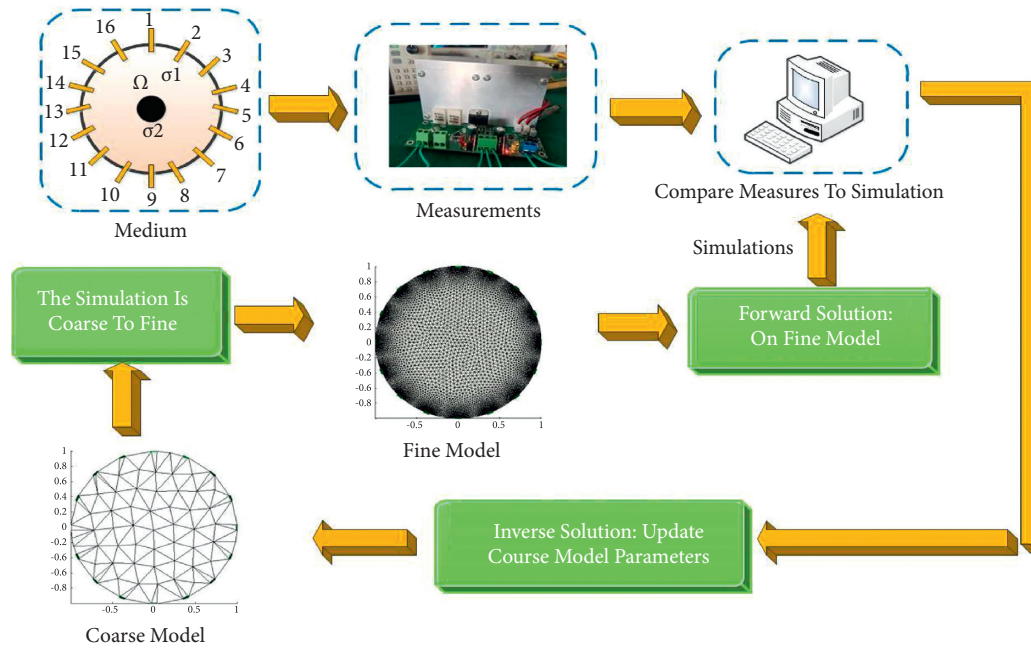


FIGURE 6: Schematic diagram for modeling the forward and reverse problems.

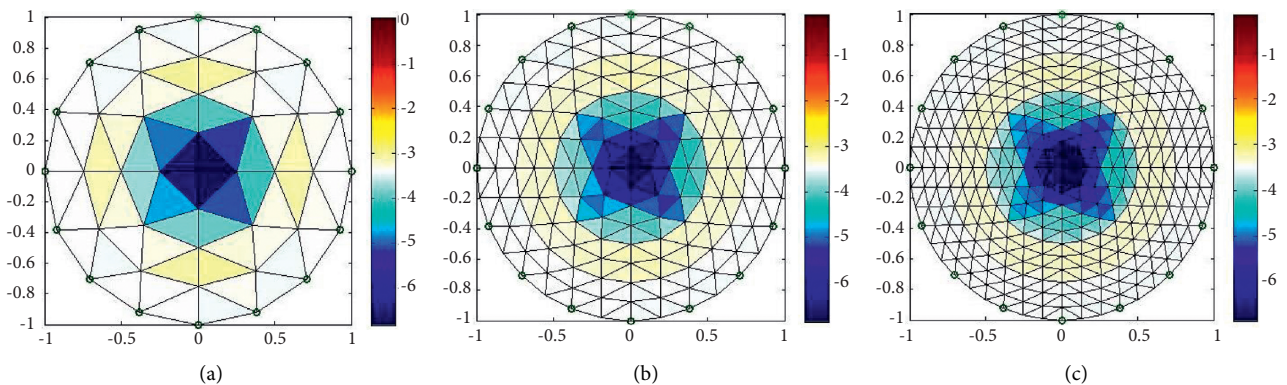


FIGURE 7: Finite element model meshing diagram.

TABLE 1: Experimental summary table.

Experimental variable	Count
1 Metal discs with different electrical conductivity	2
2 The number of electrodes compared	2
3 Number of electrodes	16
4 Number of excitation modes	8
5 Number of measurement modes	2
6 The number of reconstruction method comparisons	2
7 Alcohol burner	1
8 Location of research object	Central
9 Minimum accuracy tested	1.5% of the mental discs

TABLE 2: Experimental material size table.

Object	Measured values (mm)
1 Metal disc diameter	200
2 Round hole diameter	20
3 Electrode head diameter	2
4 Electrode end diameter	5
5 Electrode spacing	3.5

including those with industrial frequency interference, radio interference, etc., thus causing severe interference to the experimental results [45]. Therefore, this paper arranges two

steps to solve the data noise reduction problem. First, the excitation source provides a single frequency sinusoidal AC signal to complete the excitation. The excitation signal imparts a frequency signature. Figure 9 shows the excitation sensitive field potential map, where a is the electric field distribution and b is the local electrode potential line distribution.

Then, according to the frequency characteristics of the collected data, wavelet analysis is used to extract the single

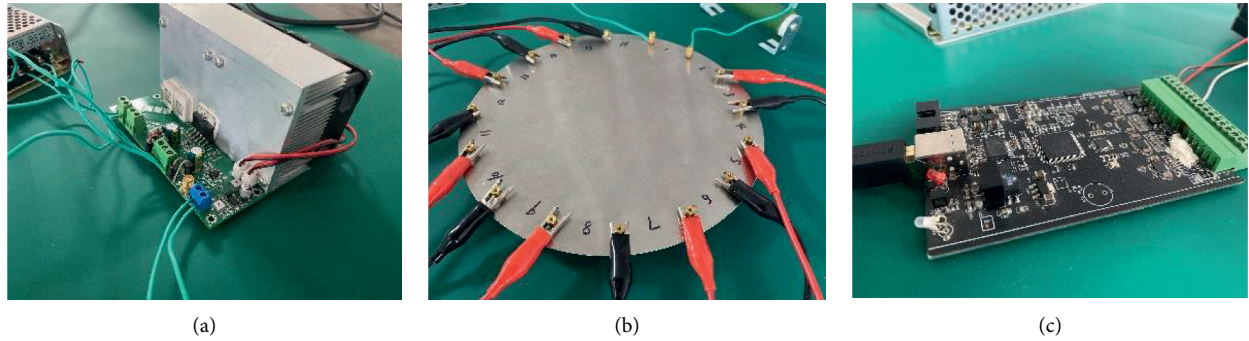


FIGURE 8: Experimental platform diagram. (a) The excitation unit; (b) the sensor electrode array; (c) the signal acquisition and processing unit.

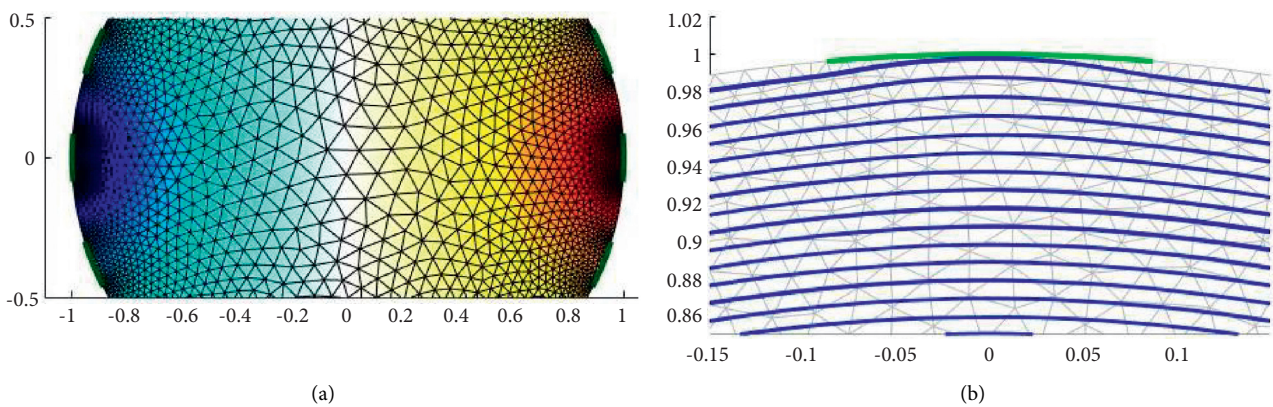


FIGURE 9: Excitation sensitive field potential diagram. (a) The electric field distribution map; (b) the local electrode potential line distribution map.

frequency excitation information and complete the noise reduction of the mixed-signal data.

Figure 10 shows the noise reduction results of the 16-electrode disc. The results show that the simulation is closer to the actual situation as the degree of noise reduction deepens. The effect of noise reduction on the data using the Shannon wavelet is apparent and provides a reliable basis for image reconstruction.

3.2.2. Relationship between the Number of Electrodes and Measurement Data. The number of sensitive field boundary electrodes is a critical factor in determining the accuracy of the data collected. The greater the number of electrodes, the greater the amount of voltage value data obtained. The more information provided in the image reconstruction, the more accurate the calculation of the resistivity distribution in the field [45]. Figure 11 shows a two-dimensional model diagram, in which *a* is the 8-electrode 2D model diagram and *b* is the 16-electrode 2D model diagram.

Figure 12 shows a graph of the measurement data of the electrode perforated disc. Figure 12(a) shows the diagram of measurement data of the 8-electrode perforated disc, and

Figure 12(b) shows the graph of measurement data of the 16-electrode perforated disc. The voltage signal data plots for the two cases of the number of excitation electrodes are compared and analyzed. After the electrodes finished excitation, the measured voltage data showed a “U” curve distribution, which was consistent with the theoretical curve of voltage signal distribution of the sensitive field electrode array arrangement.

According to the results, 16 electrodes can obtain more measurement data than eight with the same excitation pattern and medium distribution. The data are smoother and have fewer outliers, which is conducive to improving the reconstruction image quality. Moreover, the 16-electrode model has less noise and better spatial recognition of the medium distribution than the 8-electrode model. Therefore, the number of 16 electrodes selected in this paper has a good consistency and is more suitable for metal conductivity tomography imaging systems.

3.2.3. Relationship between Incentive Measurement Mode and Measurement Data. The excitation measurement mode is a crucial factor affecting the reliability of the voltage signal data of the metal structure and determines the quality of the

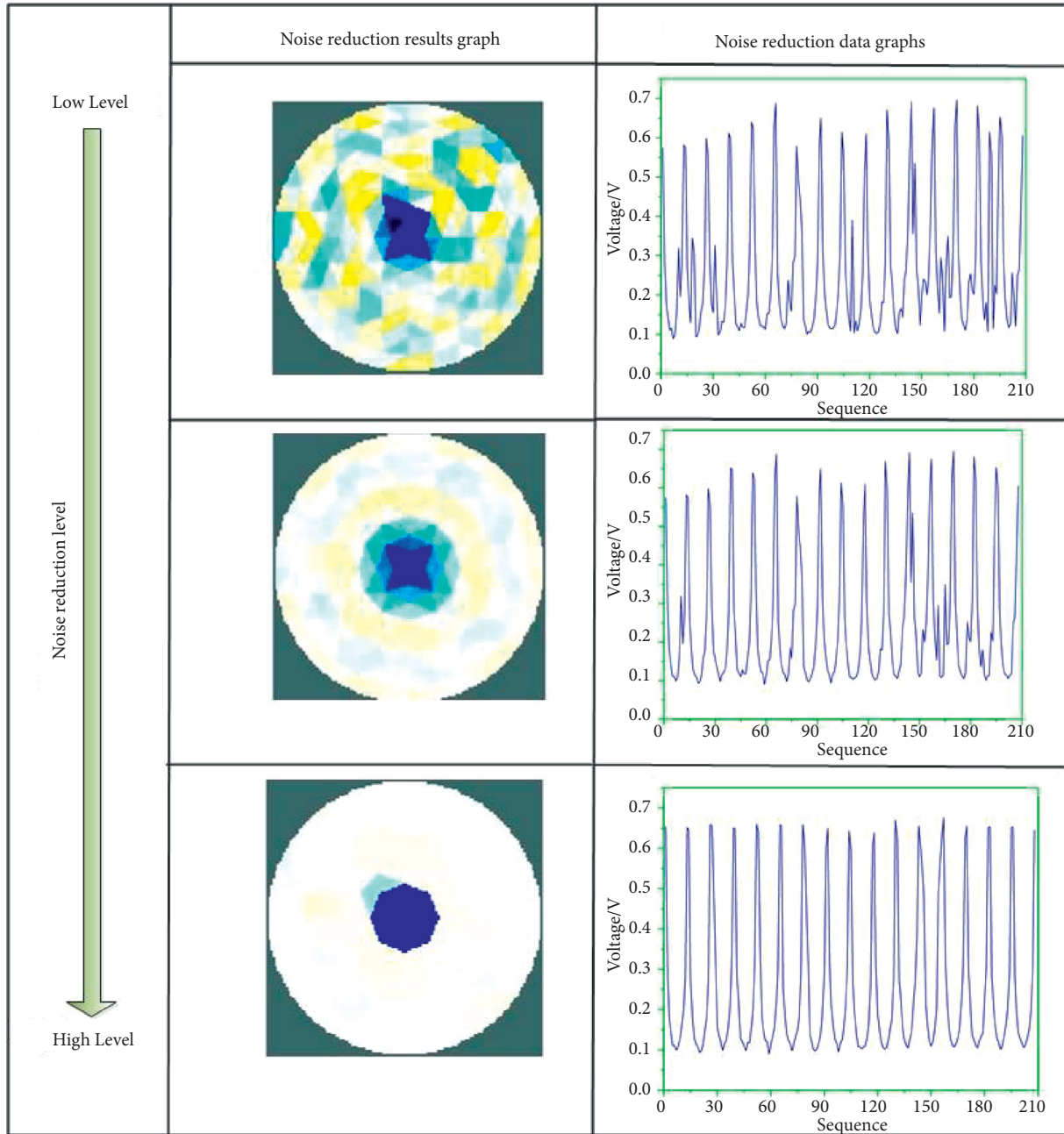


FIGURE 10: 16-electrode disc noise reduction results graph.

reconstructed image. Figure 13 shows the schematic diagram of the excitation and measurement modes. Among them, Figure 13(a) is the schematic diagram of adjacent excitation adjacent measurement; Figure 13(b) is the schematic diagram of interval excitation reference measurement. A mode of excitation current mostly passes through the field's boundary only, and the distribution of equipotential lines in the sensitive area is not uniform. B mode of excitation current passes through the centre of the field, the uniformity of current distribution is enhanced, and the amplitude of voltage value change is more significant, which is beneficial to measure the voltage signal and improve the quality of inversion imaging.

The adjacent excitation mode is defined as Mode1. Depending on the number of spaced electrodes, the spaced excitation mode is defined as Mode2-Mode8 in that order.

Table 3 shows the amount of measurement data for each excitation and measurement mode. The table shows that the reference measurement mode in the metal perforated disc measurement mode has significantly more data volume than the adjacent measurement mode. The amount of independent data is more favourable when Mode 2 to 7 interval excitation mode is used for the excitation mode. Mode1 contiguous excitation mode is the second; Mode8 relative excitation mode has the least amount of data and should be avoided as much as possible.

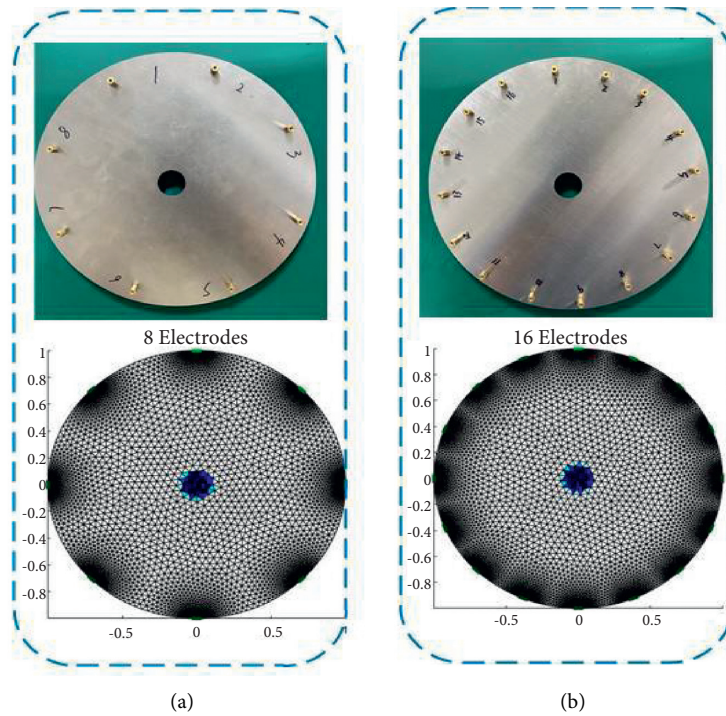


FIGURE 11: Two-dimensional model diagram: (a) 8-electrode model; (b) 16-electrode model.

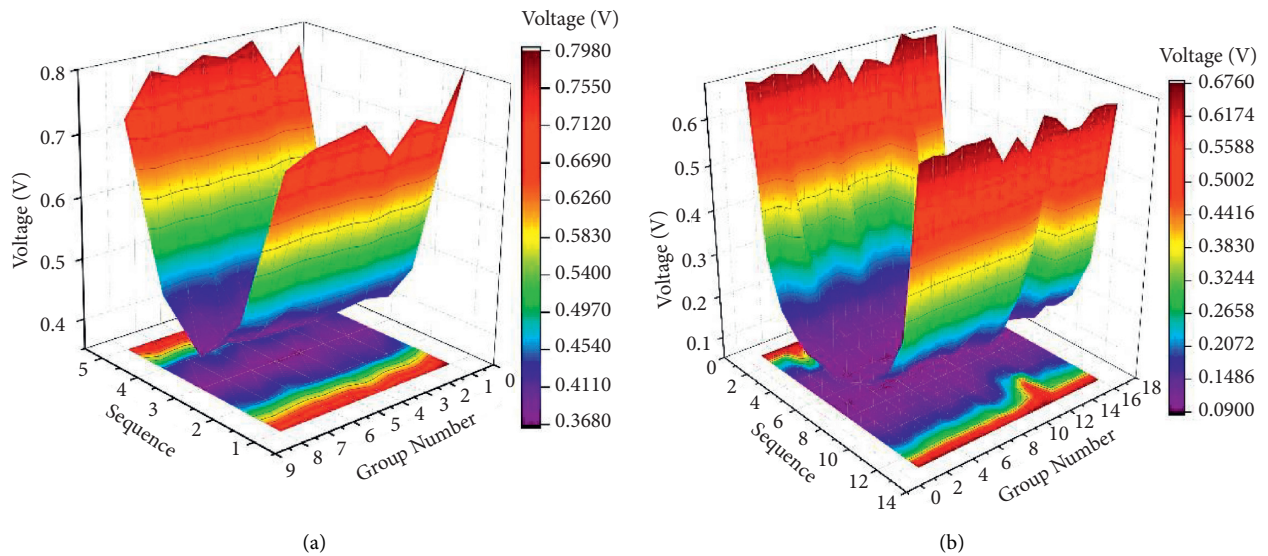


FIGURE 12: Measurement data graph. (a) A plot of 8-electrode perforated disc measurement data; (b) a story of 16-electrode perforated disc measurement data.

Figure 14 shows the measurement data plot of the perforated disc for the interval excitation reference measurement mode, and Figure 12(b) shows the measurement data plot for the adjacent excitation adjacent measurement mode. The RMS voltage data collected during the two different excitation measurement methods are compared and analyzed. Because the measurement method in Figure 14 is a reference measurement, the measurement data graph is presented as an inverted “U” shape.

Figure 15 shows the electric field diagram for each excitation mode. The figure shows that the electric field distribution is uniform as the number of electrodes spaced between the excitation electrodes increases.

According to the above results, the combination mode of Mode7 and reference measurement selected for this system can measure higher voltage values than adjacent modes. The absolute value of the measured value is significant, the current distribution is uniform, and the signal data fluctuation is slightly more stable, which is

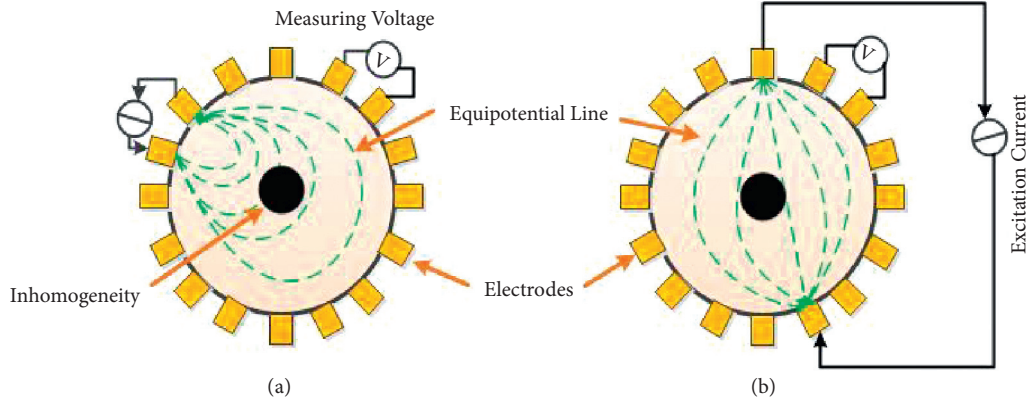


FIGURE 13: Schematic diagram of the excitation and measurement model: (a) adjacent excitation adjacent measurement; (b) interval excitation reference measurement.

TABLE 3: The amount of measurement data for each excitation and measurement mode.

Motivation model	Adjacent to measure	Reference measurement
Mode1	104	208
Mode2	192	208
Mode3	192	208
Mode4	192	208
Mode5	192	208
Mode6	192	208
Mode7	192	208
Mode8	92	104

3.2.4. *Comparative Analysis of ERT Super-Resolution Reconstructed Images.* To address the low resolution of the reconstructed image, this paper takes the low-resolution image reconstructed by the conventional Gaussian Newton algorithm as the reference basis. It uses a larger magnification of the traditional array of pixels to extract feature information. Then, the high-resolution images are reconstructed by multiple iterations to improve the quality of the reconstructed images.

Figure 16 shows the super-resolution reconstruction of the perforated disc. The results show that the Gaussian Newton method has a low similarity and is unsuitable for detecting complex, sensitive fields. The ghosting and noise of the super-resolution reconstructed image are significantly reduced. The resolution of the reconstructed image is improved considerably with the application of the super-resolution reconstruction technique, which can achieve accurate reproduction of the medium shape, size, and spatial orientation of the sensitive field fields. The following experiments will use the super-resolution method to complete the reconstructed images of 304 stainless steel temperature experiments.

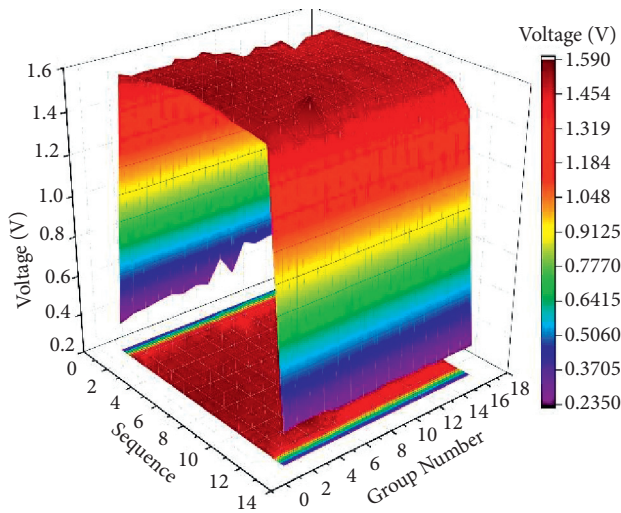


FIGURE 14: Plot of measurement data for interval excitation reference measurement mode.

conductive to improving the resolution of the inversion reconstruction image. In summary, the adjacent excitation and reference measurement mode selected in this paper is better than other excitation measurement methods and is more reasonable in practical applications.

3.3. *Results and Discussion.* In this paper, metal disc temperature experiments demonstrate the feasibility of the proposed research method and the designed ERT system in a complex environment.

Figure 17 shows the experimental test diagram. Figure 17(a) shows the experimental platform; Figure 17(b) shows the graph of the measured data of the heated disc. The ERT data acquisition unit is connected to the nonporous disc and heated at a fixed position chosen by the 304 stainless steel disc to simulate and analyze the change of resistivity distribution caused by the temperature. The actual atomic vibrations inside the metal are proportional to the temperature. When the temperature increases, the chance of collision between free electrons and real atomic increases, leading to fluctuations in the resistivity distribution, which indirectly affects the boundary voltage. The results show that the voltage near the heated region shows significant volatility relative to the specific area. The measured data follow the

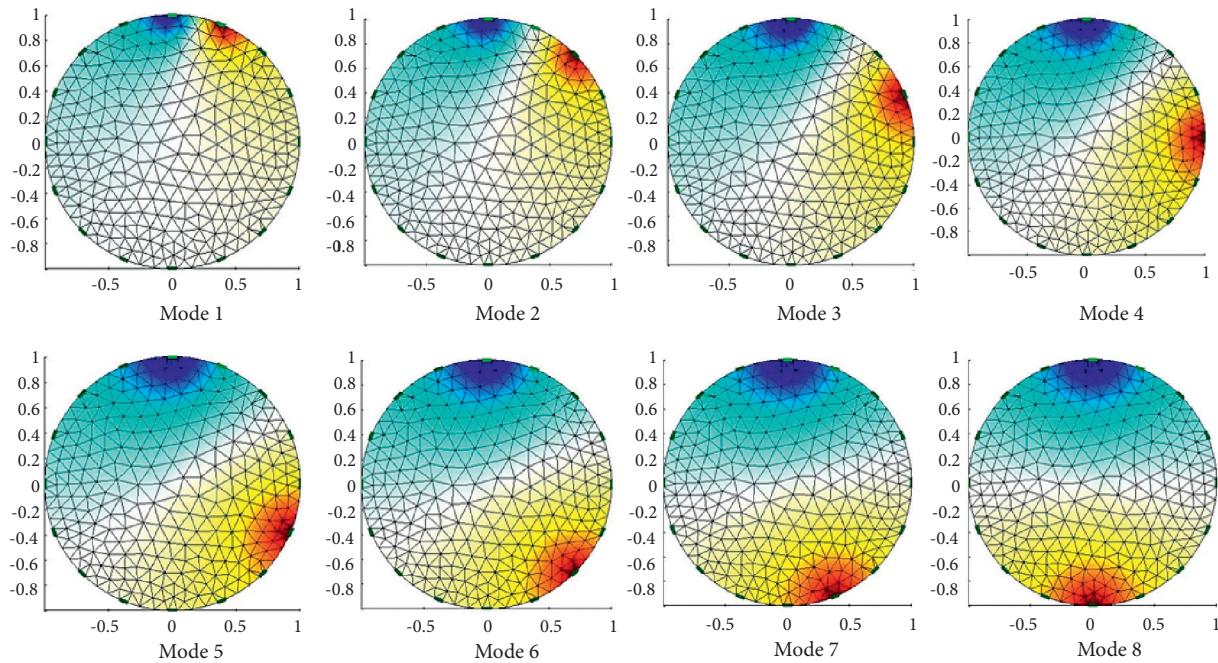


FIGURE 15: Electric field diagram for each excitation mode.

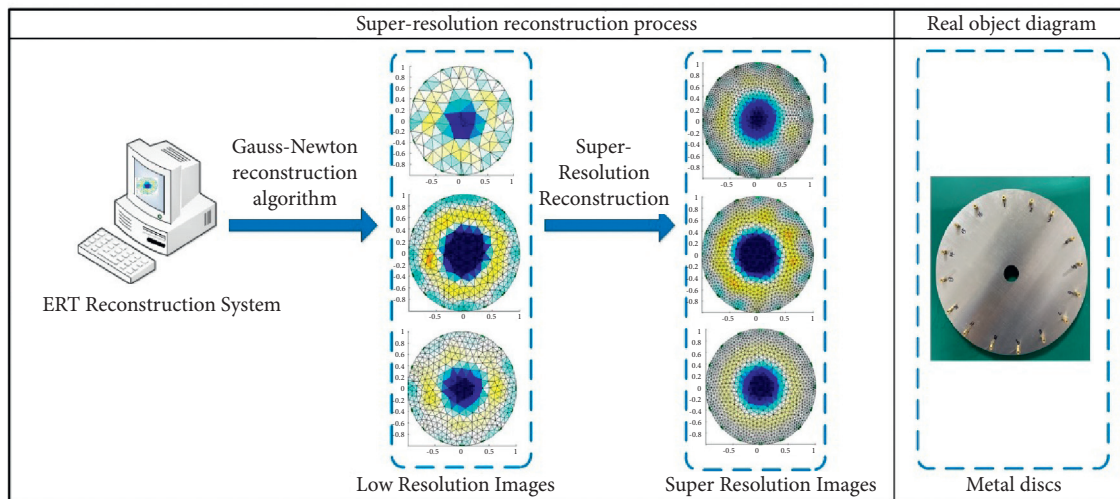


FIGURE 16: Super-resolution reconstruction of a perforated disc.

pattern, which verifies the feasibility of the ERT imaging system in terms of actual voltage data.

Figure 18 shows the temperature experiment disc reconstruction diagram. As shown in the figure, the red area indicates the heating interface. The other parts of the colour indicate the regular metal plate, which gradually expands around the red zone. On the other hand, when the heated area is close to the excitation electrode pair, the current lines pass through the site, and thus the potential values are more affected. The current line “bypasses” the heated area through the outer ring in the area of the distant electrode pair so that the resistivity of the more distant area is less affected by temperature. The location and size of the heated area shown

in the figure are generally consistent with the actual situation, which verifies the feasibility of the ERT imaging system in terms of location and size.

4. Discussion

The conductivity tomography imaging device for metal materials developed in this paper can accurately resolve the conductivity distribution of metals with high image quality accuracy. It is assumed that the accuracy of data acquisition is improved. In this case, micro-level metal conductivity distribution detection will be realized, which is essential for preventing industrial accidents. Therefore, in this paper,

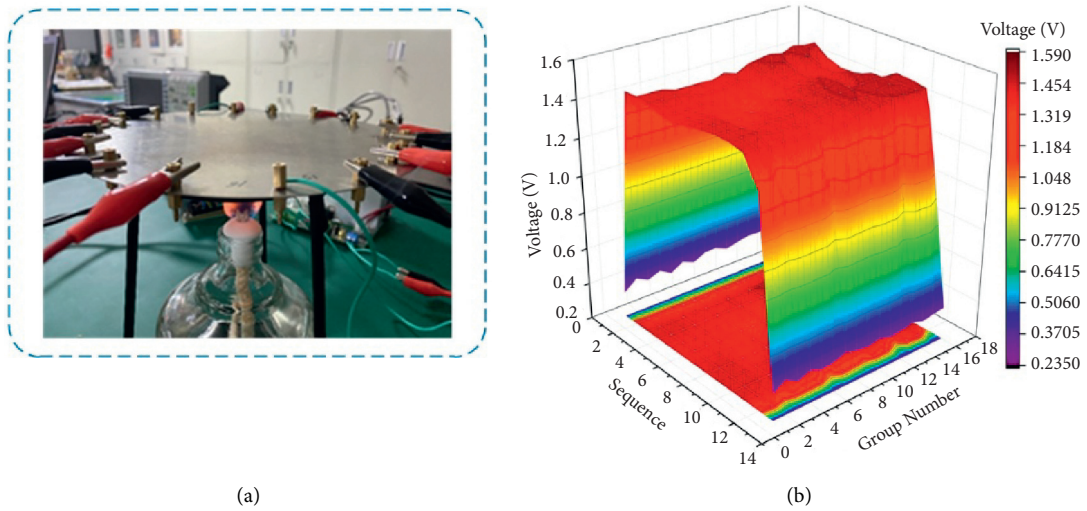


FIGURE 17: Experimental test diagram: (a) experimental platform; (b) heat-treated disc measurement data chart.

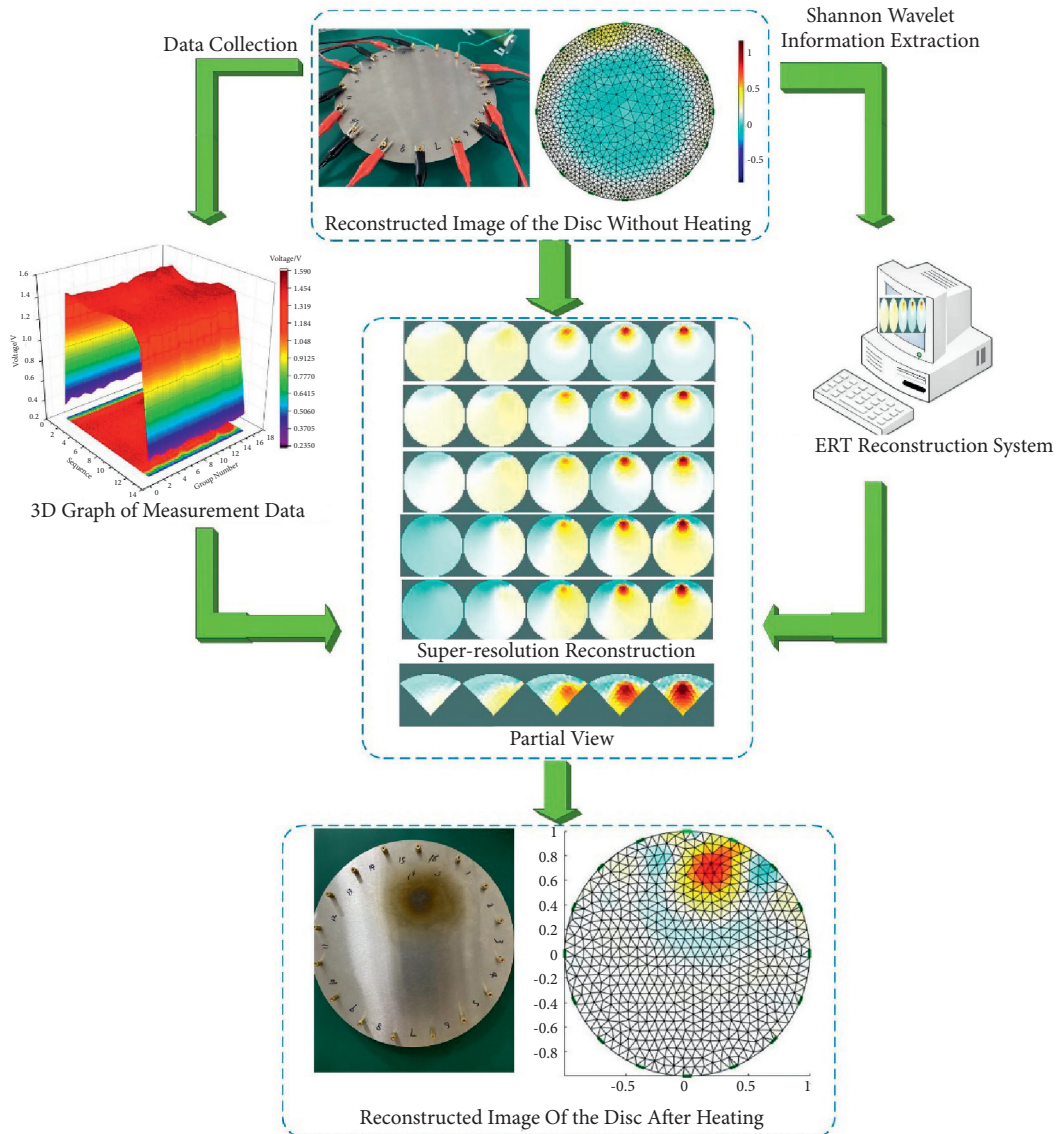


FIGURE 18: Temperature experiment disc reconstruction diagram.

future research can be conducted regarding data acquisition and processing units in the ERT system to improve the data acquisition accuracy. This research result can be applied to the crystal structure analysis of metal materials in the future, which has some commercial research value.

5. Conclusions

In this paper, a high-precision method for conductivity tomography imaging of metallic materials is proposed. At the same time, the performance of the designed metal conductivity tomography imaging equipment is thoroughly investigated in this paper, and the relationship between data noise reduction, number of electrodes, excitation measurement mode, super-resolution reconstruction method, and measurement data is discussed in detail. The research in this paper reveals the principle of excitation source to give single frequency sinusoidal AC feature signal, which provides the theoretical basis for Shannon wavelet to extract feature signal. The data noise reduction results show that the simulation effect is closer to the actual situation than the noise reduction depth. The experimental results of the number of electrodes show that 16 electrodes can obtain more measurement data. The data are smoother and with fewer outliers, conducive to improving the reconstructed image quality, and more suitable for metal conductivity tomography imaging system. The experimental results of the excitation measurement mode show that the combination mode of Mode7 and reference measurement selected for this system can measure higher voltage values than the adjacent modes. The absolute value of the measured value is significant, the current distribution is uniform, and the signal data fluctuation is slightly more stable, which is conducive to improving the resolution of the inverse reconstructed image. The super-resolution image reconstruction method takes the low-resolution image reconstructed by the traditional Gaussian Newton algorithm as the reference basis. It then reconstructs the high-resolution image by multiple iterations. The experimental results of super-resolution reconstructed images show that the ghosting and noise of super-resolution reconstructed images are significantly reduced, which effectively solves the low resolution of reconstructed images of conductivity distribution of metal materials. Finally, the temperature experiment verifies the feasibility of the high-precision laminar imaging method for metallic materials proposed in this paper. The results show that the voltage near the heated region shows significant voltage fluctuations compared to the specific area. The measured data are by the pattern, which verifies the feasibility of the ERT imaging system in terms of the actual voltage data. The location and size of the heated area shown in the figure are generally consistent with the actual situation, which verifies the feasibility of the ERT imaging system in terms of location and size.

In conclusion, based on a series of experiments, it can be concluded that the experimental platform built in this paper can detect and visualize the electrical conductivity distribution of metals. The proposed method of metal conductivity detection can be used as a reference for the study of

metal processing. Studying the relationship between crystal structure changes and electrical conductivity has good application prospects for improving the processing process. In conclusion, this study can be applied to structural defect detection and conductivity analysis of large metal parts and lays the foundation for using resistive tomography in the direction of metallic materials.

Data Availability

The data presented in this study are available on request from the corresponding author. The data are not publicly available due to restrictions, e.g., privacy or ethical.

Disclosure

The funding sponsors had no role in the design of the study; in the collection, analyses, or interpretation of data; in the writing of the manuscript; or in the decision to publish the results.

Conflicts of Interest

The authors declare no conflicts of interest.

Acknowledgments

This research was funded by Shaanxi Provincial Key Research and Development Program, Grant no. 2020ZDLGY04-06, and by Shaanxi Provincial Key Research and Development Program, Grant no. 2019ZDLGY03-09-02. The work was also supported by the Natural Science Foundation of Shaanxi Province, Grant no. 2020JM-529, and the Natural Science Foundation of Shaanxi Province Shaanxi Coal Joint Fund Project, Grant no. 2021JLM-08.

References

- [1] H. Mao, X. Yi, H. Mao et al., "Fatigue damage detection and location of metal materials by electrical impedance tomography," *Results in Physics*, vol. 15, Article ID 102664, 2019.
- [2] T. d. C. Martins, A. K. Sato, F. S. d. Moura et al., "A review of electrical impedance tomography in lung applications: Theory and algorithms for absolute images," *Annual Reviews in Control*, vol. 48, pp. 442–471, 2019.
- [3] K. C. Mandal, J. W. Kleppinger, and S. K. Chaudhuri, "Advances in high-resolution radiation detection using 4H-SiC epitaxial layer devices," *Micromachines*, vol. 11, no. 3, p. 254, 2020.
- [4] J. M. Milne and P. Carter, "A transient thermal method of measuring the depths of sub-surface flaws in metals," *British Journal of Non-destructive Testing*, vol. 30, no. 5, pp. 333–336, 1988.
- [5] S. Zhao, M. Wei, C. Zhang, W. Guo, and Z. Lu, "Coal mine inclined shaft advanced detection method and physical model test based on shield cutterhead moving array electrodes," *Energies*, vol. 12, no. 9, p. 1671, 2019.
- [6] Z. Xing, S. Zhao, W. Guo, X. Guo, and Y. Wang, "Processing laser point cloud in fully mechanized mining face based on DGCNN," *ISPRS International Journal of Geo-Information*, vol. 10, no. 7, p. 482, 2021.

- [7] Q. Wang, J. He, J. Wang et al., "An image reconstruction algorithm for electrical impedance tomography using Symkaczmarz based on structured sparse representation," *Transactions of the Institute of Measurement and Control*, vol. 41, no. 10, pp. 2803–2815, 2019.
- [8] R. Saad, M. N. M. Nawawi, and E. T. Mohamad, "Groundwater detection in alluvium using 2-D electrical resistivity tomography (ERT)," *Electronic Journal of Geotechnical Engineering*, vol. 17, pp. 369–376, 2012.
- [9] T. Rymarczyk, P. Adamkiewicz, K. Duda, J. Szumowski, and J. Sikora, "New electrical tomographic method to determine dampness in historical buildings[[]]," *Archives of Electrical Engineering*, vol. 65, no. 2, pp. 273–283, 2016.
- [10] A. Kemna, J. Vanderborght, B. Kulesa, and H. Vereecken, "Imaging and characterisation of subsurface solute transport using electrical re-sistivity tomography (ERT) and equivalent transport models," *Journal of Hydrology*, vol. 267, no. 3-4, pp. 125–146, 2002.
- [11] J. Koestel, A. Kemna, M. Javaux, A. Binley, and H. Vereecken, "Quantitative imaging of solute transport in an unsaturated and undisturbed soil monolith with 3-D ERT and TDR," *Water Resources Research*, vol. 44, no. 12, 2008.
- [12] M. Sharifi and B. Young, "Electrical resistance tomography (ERT) applications to chemical engineering," *Chemical Engineering Research and Design*, vol. 91, no. 9, pp. 1625–1645, 2013.
- [13] Z. J. Yang and G. Yan, *Detection of Impact Damage for Composite Structure by Electrical Impedance Tomography*, Springer, New York, NY, USA, 2020.
- [14] H. Ghaednia, C. E. Owens, R. Roberts, T. N. Tallman, A. J. Hart, and K. M. Varadarajan, "Interfacial load monitoring and failure detection in total joint replacements via piezoresistive bone cement and electrical impedance tomography," *Smart Materials and Structures*, vol. 29, no. 8, Article ID 085039, 2020.
- [15] Y. Zhu and Z. Wang, "Measurement of soil resistivity based on FFT DC component," *Optics and Precision Engineering*, vol. 21, no. 1, pp. 115–123, 2013.
- [16] K. Karhunen, A. Seppänen, A. Lehtikoinen, P. J. M. Monteiro, and J. P. Kaipio, "Electrical resistance tomography imaging of concrete," *Cement and Concrete Research*, vol. 40, no. 1, pp. 137–145, 2010.
- [17] G. Rao, M. A. Sattar, R. Wajman, and L. Jackowska-Strumillo, "Application of the 2D-ERT to evaluate phantom circumscribed regions in various sucrose solution concentrations," in *Proceedings of the 2019 International Interdisciplinary PhD Workshop (IIPhDW)*, pp. 34–38, IEEE, Wismar, Germany, May 2019.
- [18] G. Rao, S. Aghajanian, T. Koiranen, R. Wajman, and L. Jackowska-Strumillo, "Process monitoring of antisolvent based crystallization in low conductivity solutions using electrical impedance spectroscopy and 2-D electrical resistance tomography," *Applied Sciences*, vol. 10, no. 11, p. 3903, 2020.
- [19] L. Boulanger, "Observations on variations in electrical conductivity of pure demineralized water: modification ("activation") of conductivity by low-frequency, low-level alternating electric fields," *International Journal of Biomeeteorology*, vol. 41, no. 3, pp. 137–140, 1998.
- [20] K. Hornik, M. Stinchcombe, and H. White, "Multilayer feedforward networks are universal approximators," *Neural Networks*, vol. 2, no. 5, pp. 359–366, 1989.
- [21] V. Kolehmainen, M. Lassas, M. Lassas, P. Ola, and S. Siltanen, "Recovering boundary shape and conductivity in electrical impedance tomography," *Inverse Problems and Imaging*, vol. 7, no. 1, pp. 217–242, 2013.
- [22] S. Ciulli, M. K. Pidcock, and C. Sebu, "An integral equation method for the inverse conductivity problem," *Physics Letters A*, vol. 325, no. 3-4, pp. 253–267, 2004.
- [23] J. Santana Martins, C. Stein Moura, and R. M. Figueiró Vargas, "Avaliação de 3 diferentes aproximações para a solução do problema direto da tomografia de impedância elétrica," *Revista Internacional de Métodos Numéricos para Cálculo y Diseño en Ingeniería*, vol. 31, no. 1, pp. 42–49, 2015.
- [24] M. Zhang and M. Soleimani, "Imaging floating metals and dielectric objects using electrical capacitance tomography," *Measurement*, vol. 74, pp. 143–149, 2015.
- [25] L. Xiao, H. Wang, and X. Xu, "Improved Newton-raphson algorithm for electrical resistance tomography image reconstruction. Zhongguo dianji gongcheng xuebao (proceedings of the Chinese society of electrical engineering)," *Chinese Society for Electrical Engineering*, vol. 32, no. 8, pp. 91–97, 2012.
- [26] M. Sharifi and B. Young, "Electrical resistance tomography (ERT) for flow and velocity profile measurement of a single phase liquid in a horizontal pipe," *Chemical Engineering Research and Design*, vol. 91, no. 7, pp. 1235–1244, 2013.
- [27] O. Dorn, E. L. Miller, and C. M. Rappaport, "A shape reconstruction method for electromagnetic tomography using adjoint fields and level sets," *Inverse Problems*, vol. 16, no. 5, pp. 1119–1156, 2000.
- [28] J. Wu, "The applied technology of time resolved ultrasonic flow meter," *Sci-Tech & Development of Enter-Prise*, vol. 2, pp. 16–20, 2010.
- [29] T. De Castro Martins, E. D. L. Bueno de Camargo, R. Gonzalez Lima, M. B. P. Amato, and M. de Sales Guerra Tsuzuki, "Image reconstruction using interval simulated annealing in electrical impedance tomography," *IEEE Transactions on Biomedical Engineering*, vol. 59, no. 7, pp. 1861–1870, 2012.
- [30] Z. Huang, D. Xie, H. Zhang, and H. Li, "Gas-oil two-phase flow measurement using an electrical capacitance tomography system and a Venturi meter," *Flow Measurement and Instrumentation*, vol. 16, no. 2-3, pp. 177–182, 2005.
- [31] M. Wang and X. Zhong, "Applied research on time difference method in ultrasonic gas flow meter," *Instrument Technique and Sensor*, vol. 7, pp. 26–28, 2013.
- [32] K. S. Kuo-Sheng Cheng, D. Isaacson, J. C. Newell, and D. G. Gisser, "Electrode models for electric current computed tomography," *IEEE Transactions on Biomedical Engineering*, vol. 36, no. 9, pp. 918–924, 1989.
- [33] J. Ye, H. Wang, and W. Yang, "A sparsity reconstruction algorithm for electrical capacitance tomography based on modified Landweber iteration," *Measurement Science and Technology*, vol. 25, no. 11, Article ID 115402, 2014.
- [34] C. W. Groetsch and C. W. Groetsch, *Inverse Problems in the Mathematical Sciences*, Vieweg, Braunschweig, Germany, 1993.
- [35] B. S. Kim, S. Kim, and K. Y. Kim, "Image reconstruction with prior information in electrical resistance tomography," *Journal of IKEEE*, vol. 18, no. 1, pp. 8–18, 2014.
- [36] W. ChuanLei and Y. ShiHong, "New selection methods of regularization parameter for electrical resistance tomography image reconstruction," in *Proceedings of the 2016 IEEE International Instrumentation and Measurement Technology Conference Proceedings*, pp. 1–5, IEEE, Taipei, Taiwan, May 2016.

- [37] F. Dickin and M. Wang, "Electrical resistance tomography for process applications," *Measurement Science and Technology*, vol. 7, no. 3, pp. 247–260, 1996.
- [38] B. S. Kim, A. K. Khambampati, S. Kim, and K. Y. Kim, "Image reconstruction with an adaptive threshold technique in electrical resistance tomography," *Measurement Science and Technology*, vol. 22, no. 10, Article ID 104009, 2011.
- [39] M. Vauhkonen, W. R. B. Lionheart, L. M. Heikkinen, P. J. Vauhkonen, and J. P. Kaipio, "A MATLAB package for the EIDORS project to reconstruct two-dimensional EIT images," *Physiological Measurement*, vol. 22, no. 1, pp. 107–111, 2001.
- [40] A. Adler and W. R. B. Lionheart, "Uses and abuses of EIDORS: an extensible software base for EIT," *Physiological Measurement*, vol. 27, no. 5, pp. S25–S42, 2006.
- [41] N. Polydorides and W. R. B. Lionheart, "A Matlab toolkit for three-dimensional electrical impedance tomography: a contribution to the Electrical Impedance and Diffuse Optical Reconstruction Software project," *Measurement Science and Technology*, vol. 13, no. 12, pp. 1871–1883, 2002.
- [42] P. Yan and Y. Mo, "Imaging the complex conductivity distribution in electrical impedance tomography," *IFAC Proceedings Volumes*, vol. 36, no. 15, pp. 73–76, 2003.
- [43] B. S. Kim, A. K. Khambampati, Y. J. Jang, K. Y. Kim, and S. Kim, "Image reconstruction using voltage-current system in electrical impedance tomography," *Nuclear Engineering and Design*, vol. 278, pp. 134–140, 2014.
- [44] M. Soleimani, W. R. B. Lionheart, and O. Dorn, "Level set reconstruction of conductivity and permittivity from boundary electrical measurements using experimental data," *Inverse Problems in Science and Engineering*, vol. 14, no. 2, pp. 193–210, 2006.
- [45] C. Luo, W. He, and X. Dong, "Driven patterns with fixed excitation in electrical impedance tomography," *Chinese Journal of Biomedical Engineering*, vol. 28, no. 6, pp. 949–953, 2009.